Critical Test of the Validity of Monin–Obukhov Similarity during Convective Conditions

CECILIA JOHANSSON, ANN-SOFI SMEDMAN, AND ULF HÖGSTRÖM

Department of Earth Sciences, Meteorology, Uppsala University, Uppsala, Sweden

JAMES G. BRASSEUR AND SAMIR KHANNA*

Department of Mechanical Engineering, The Pennsylvania State University, University Park, Pennsylvania

(Manuscript received 27 July 1999, in final form 14 June 2000)

ABSTRACT

A recent study of convective boundary layer characteristics performed with large eddy simulation technique (LES) has demonstrated unexpected influence of the depth of the boundary layer on surface layer characteristics. The present study tests some of the predictions from these simulations with field measurements from a summertime experiment in Sweden, which includes in addition to regular surface layer data also airborne measurements and numerous radio soundings, which enable accurate determination of boundary layer depth.

It is found that the measurements strongly support most of the conclusions draws from the LES study and give additional information over a wider stability range. Thus, the normalized wind gradient ϕ_m is found to depend on both z/L, where z is height above the ground and L is the Monin–Obukhov length, and z_i/L, where z_i is the height of the convective boundary layer. This additional dependence on z_i/L explains much of the scatter between experiments encountered for this parameter. In the case of the normalized temperature gradient ϕ_h, the experimental data follow the generally accepted functional relation with z/L, but with an additional, slight ordering according to z_i/L.

Analyses of nondimensional variances show (i) the horizontal velocity variance scales on mixed layer variables and is a function only of z_i/L, in agreement with the LES results and with previous measurements; (ii) the normalized vertical velocity variance depends on the large-scale pressure gradient length scale for slight instability and is primarily a function of z/L for moderate and strong instability; (iii) the normalized temperature variance is a function of z/L, with a possible slight dependence on z_i/L; and (iv) whereas mean temperature gradient is characterized by local shear scales, temperature variances are normalized by local buoyancy-driven scales.

1. Introduction

The Monin-Obukhov theory has been considered the backbone of surface layer meteorology since it was first presented in a series of papers about 50 yr ago by Obukhov (1946), Monin (1950), and Monin and Obukhov (1953, 1954). As detailed in section 2, the theory essentially predicts that statistical quantities in the surface layer are properly normalized by the velocity scale $u_* = \sqrt{(-\overline{u'w'})_0}$, where $(-\overline{u'w'})_0$ is the kinematic momentum flux at the surface; the temperature scale $T_* = -Q_0/u_*$, where Q_0 is the temperature flux $(\overline{w'\theta'})_0$ at the surface; and the height above the ground z, and that the quantities normalized with these parameters are unique functions of the dimensionless height z/L, where

$$L = -\frac{u_*^3 T_0}{kgQ_0} \tag{1}$$

is the Monin–Obukhov length, with T_0 = the mean temperature of the surface layer in Kelvin, k = the von Kármán constant = 0.4, and g = acceleration of gravity = 9.81 m s^{-2}. In this form the theory is strictly valid for dry air. For moist air, the flux of virtual temperature replaces the ''ordinary'' temperature flux (cf. section 3e below).

In numerical meteorological models on all scales, from local and mesoscale models to global models, Monin–Obukhov formulations are used to relate surface fluxes of momentum, sensible heat, and water vapor to bulk meteorological parameters. Predictions from the theory have been the subject of innumerable field tests throughout the years, as reviewed recently by Högström (1996). Because of statistically incomplete sampling (Lumley and Panofsky 1964; Dyer et al. 1982; Högström 1988), in addition to imprecise measurement of L and other relevant parameters, possible nonequilibrium effects, and other inhomogeneity scales, statistics from

* Current affiliation: Corning, Inc., Corning, New York.

Corresponding author address: Prof. Ulf Högström, Department of Earth Sciences, Meteorology, Villavägen 16, S-752 36 Uppsala, Sweden.
E-mail: ulf@big.met.uu.se

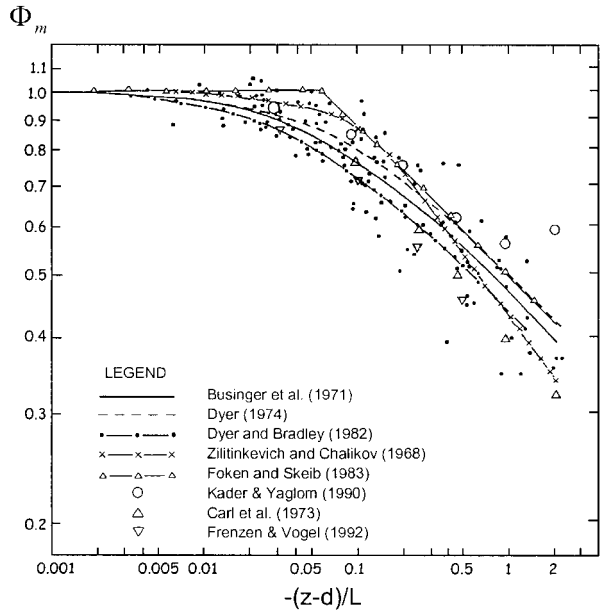

FIG. 1. Plot of the nondimensional wind gradient ϕ_m against $-(z - d)/L$ (where d is zero plane displacement) in log–log representation for unstable stratification. The small dots are 30-min mean data from Högström (1988). The other symbols have been derived from modified expressions from sources listed in the legend. Note that these data each represent mean results from individual field experiments, based in turn on a large number of typically 30-min ''runs'' [after Högström (1996)].

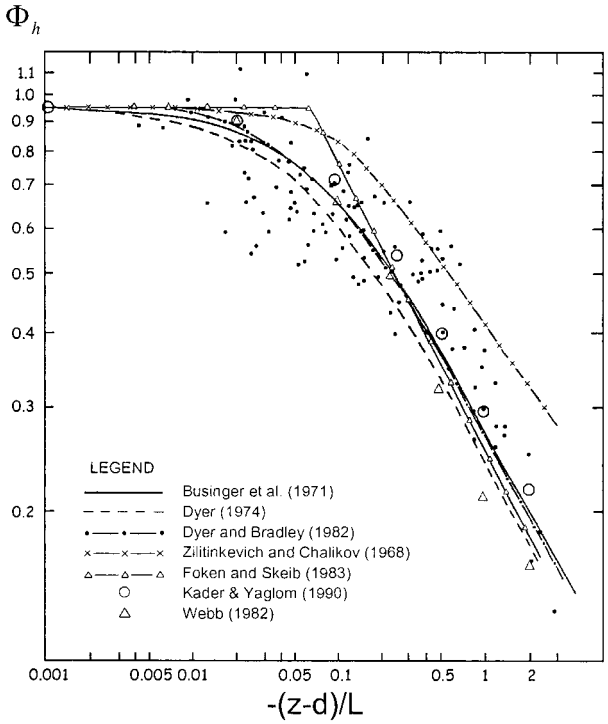

FIG. 2. As in Fig. 1 but for the nondimensional temperature gradient ϕ_h [after Högström (1996)].

individual field experiments generally contain a considerable degree of scatter. Furthermore, when mean data from several field experiments are compared, notable differences are often found.

Figures 1 and 2, which are taken from Högström (1996) illustrate this point. These show, respectively, the nondimensional wind gradient $\phi_m = (kz/u_*)\partial U/\partial z$ [where k is von Kármán's constant ≈ 0.4 and $U = U(z)$ is the mean wind speed at height z] and the nondimensional temperature gradient $\phi_h = (kz/T_*)\partial\Theta/\partial z$ [where $\Theta = \Theta(z)$ is mean potential temperature at z] as a function of $-z/L$ [actually $-(z - d)/L$, where d is zero plane displacement] illustrate this point. Except for the small black dots, which show individual half-hourly data from one particular experiment, the Lövsta experiment (Högström 1988), the various symbols show *mean* results from a number of field experiments. Particularly in the variation of ϕ_m in Fig. 1, there is considerable scatter among the mean results. The question then arises about the cause of this scatter. Högström (1996) lists a number of possible reasons, including systematic instrumental errors not adequately corrected and inadequate upwind fetch. As with most authors, Högström (1996) ruled out limitations in the validity of the Monin-Obukhov similarity theory as a possible cause for scatter.

Previous studies have, however, identified surface layer parameters that do in fact not obey this scaling. The first field data were probably presented by Kaimal et al. (1972), who found for the low-frequency part of spectra for the horizontal wind components and temperature that ''the unstable spectra are confined to the strippled area (a certain area in their logarithmic plots of the spectra) with no particular regard to z/L.'' They argued that eddies of boundary layer size were likely to influence the flow close to the ground, in agreement with Deardorff's (1972) numerical simulation results. Panofsky et al. (1977) showed in a convincing way with data from several sources that the standard deviations of the horizontal wind components normalized by the friction velocity are indeed a function of z_i/L, where z_i is the height of the boundary layer and independent of z. Experimental evidence to this effect has also been presented by Banta (1985). A physically plausible explanation for these nonlocal effects of mixed layer scales on surface layer eddies is given by Hunt et al. (1988), who argue that the large thermal plumes are formed in the mixed layer and that these plumes effectively act as non-Gaussian free stream turbulence in the surface layer.

The present study has its origin in results from recent large-eddy simulations (LESs) of the convective and near-neutral boundary layer by Khanna and Brasseur (1997), referred to as KB97 below, which indicate influences of z_i/L in certain surface layer characteristics, which have not been identified earlier. Perhaps, the most remarkable finding of that study is the prediction that ϕ_m should be a function of both z/L and z_i/L. In fact, comparing the plot for ϕ_m (Fig. 1) with that for ϕ_h (Fig. 2) shows a striking difference in scatter among the re-

spective mean curves: taking away the Zilitinkevich and Chalikov (1968) curve from the ϕ_h plot (which gives the impression of being an outlier) leaves a scatter among the remaining seven datasets (including the mean of the Lövsta data), which is only half that of the corresponding scatter in the ϕ_m plot. Such increased scatter in the mean results is what might be expected if another parameter like z_i/L is involved. If this is the case, then even after averaging within individual experiments, there would remain a certain influence of differing stability states between the experiments.

In most surface layer experiments information about the boundary layer height is missing, so that it is impossible to test such deviations from Monin–Obukhov theory (MO theory) as discussed above. In this paper data from two summertime field campaigns in southern Sweden, which contain both ordinary surface layer data (profiles and turbulent fluxes) and detailed information on boundary layer height, have been used for such a test. The field experiments are CFE1 and CFE2 (CFE = concentrated field effort) of the Northern Hemisphere Climate Processes Land Surface Experiment project (NOPEX), which were carried out during the summers of 1994 and 1995 in the NOPEX area (Halldin et al. 1998).

An advantage of simulation is the control over horizontal homogeneity and boundary conditions. Furthermore, carefully done LES provides both excellent statistical sample for well-defined equilibrium states and the three-dimensional structure, which underlies statistical sample. With LES, statistics are obtained as a function of z for fixed z_i and a few different L. Thus only a few stability states z_i/L are generally possible with LES, and variable z/L is obtained by varying z for fixed L. By contrast, field data are generally obtained at fixed z and many different z_i and L.

Whereas LES has the advantage that statistics are obtained over the entire range of z levels from near the surface to beyond that capping inversion, LES is limited in its inability to resolve with good accuracy to the very small z/z_i levels obtained in the field. In the effective 256^3 simulations of KB97, data at z levels below $z_r/z_i \approx 0.04$ are treated with some scepticism. To explore potential collapse of statistics under MO scaling requires data over a range of $-z/L$ ''small'' relative to 1. For a range z_r to $2z_r$ (where z_r is the height above which the simulations are ''well resolved'') with $z_r/L > -0.1$, say, the largest $-z_i/L$ with 256^3 LES useful for MO analysis is roughly 10. Thus, in KB97 z_i/L states -0.44, -3, and -8 were analyzed.

Our experimental data have the great advantage of being in the real atmosphere, so questions of validity rest primarily on the accuracy of the measured parameters such as z_i, u_*, Q_0, T_*, and L, and on concerns of nonequilibrium atmospheric boundary layer behavior during the daytime increase in z_i. The great advantage of the experimental data is the very wide range of z_i/L and z/L measured. The disadvantage is that the accuracy of z_i and L is not as good as in the simulations, and there is consequent scatter in the data.

An important consequence of the different conditions under which our respective data can be analyzed is that the range of z_i/L (<-60 to -0.5) of the experimental data is much more extended than those of the LES (-0.44, -3, -8), while the LES z_i/L values are more precise. Comparisons between the LES and fields data must be made with these differences in mind. It is of particular value that trends observed in the LES can be extended to higher z_i/L with field data.

The LESs that are the starting point of the present study are outlined in section 2 together with the general theoretical framework. In section 3 the measurements and evaluation procedures are described. The results of the analysis of the field data are presented in section 4, followed by discussion and conclusion in section 5.

2. The large-eddy simulations and general theoretical framework

a. Scaling arguments and KB97 summary

Scaling theories are based on the assumption that a small number of length, velocity, time, and temperature scales dominate the statistical structure of a turbulent flow within ranges of relevant nondimensional parameters and within certain regions of the flow. The adequacy of the assumptions and corresponding accuracy of the theory must, ultimately, be determined by experiment. If successful, the scalings provide a framework for organizing the statistical structure of the turbulent flow in the parameter ranges and flow regions validated.

The Monin–Obukhov similarity theory was designed to organize the statistical structure of an atmospheric surface layer driven by shear and modulated by buoyancy, that is when $-z_i/L$ is not too large (buoyancy dominated throughout) or too small (shear dominated throughout), relative to 1. The theory then applies in two overlapping layers adjacent to the ground: 1) a region $z \ll z_i$ where the surface exerts a direct influence, through continuity, forcing a reduction in integral scales roughly proportional with z (Hunt 1984; Peltier et al. 1996), and 2) a region $z < -L$ in which turbulence production is dominated by shear, where the Monin–Obukhov length [Eq. (1)] roughly identifies the height above which buoyancy production dominates shear production of turbulent kinetic energy. The friction velocity u_* characterizes shear-induced vertical momentum flux, g/T_0 paramaterizes the buoyancy force in the Navier–Stokes equation, and Q_0 (temperature flux) describes the rate of heat generation at the ground.

The shear-induced turbulent motions near the ground ($z \ll z_i$ and $z < -L$) are characterized by length and velocity scales z and u_*. Temperature fluctuations driven vertically from the ground by shear-generated turbulent velocity fluctuations are characterized by the tempera-

ture scale $T_* = -Q_0/u_*$. On the other hand, the mixed layer ($z > -L$) is dominated by buoyancy-driven motions originating at the ground but bounded by the capping inversion. Thus, the most energetic buoyancy-induced motions are characterized by length scale z_i, velocity scale $w_* = [(g/T_0)Q_0 z_i]^{1/3}$, and temperature scale $\Theta_* = -Q_0/w_*$. However, in the region of ground influence, vertical velocity fluctuations are damped, so that buoyancy-dominated *vertical* motions at $z \ll z_i$ are characterized by the ''free convection'' length and velocity scales z and $u_f(z) = [k(g/T_0)Q_0 z]^{1/3}$. Temperature fluctuations driven vertically from the ground by buoyancy-generated turbulent velocity fluctuations are characterized by the free convection temperature scale $T_f(z) = -Q_0/u_f = -[k\{(g/T_0)/Q_0^2\}z]^{-1/3}$.

Whereas in the mixed layer z_i, w_*, and Θ_* are the only characteristic large-eddy turbulence scales, in the surface layer both shear-induced scales u_*, T_*, and buoyancy-induced scales u_f, T_f potentially contribute to turbulence integral-scale structure. Furthermore, it is now well established that horizontal motions near the ground are strongly influenced by the energetic outer-scale convective motions characterized by the mixed layer scales z_i and w_* (Deardorff 1972; Panofsky et al. 1977; Kaimal 1978).

Monin–Obukhov similarity assumes that the statistical structure of the near-surface region($z \ll z_i$, $z < -L$) is dominated by the integral length scale z, the shear-induced velocity scale u_*, and the temperature scale T_*, which characterizes temperature flux by shear-induced motions. If this is the case, then a statistical turbulence quantity f must have two characteristics: 1) a scale $f_{\rm MO}$ can be formed from the variables z, u_*, and T_* which normalizes f [i.e., which makes $f/f_{\rm MO} \approx O(1)$], and 2) the normalized f should be a function only of the distance from the ground relative to the Monin-Obukhov length L. That is, MO similarity states

$$\frac{f}{f_{\rm MO}} = \Phi_f\left(\frac{z}{L}\right) \approx O(1). \tag{2}$$

In the fully shear-dominated, or neutral limit ($-z_i/L \to 0$), L is no longer a relevant scale. In this case, buoyancy forces (and consequent scales u_f, T_f) are inactive, and when $-z_i/L \ll 1$ but finite, Q_0 is a passive source of passive temperature fluctuations, and f is normalized by z, u_*, and T_* such that $f/f_{\rm MO} \approx$ constant.

In the buoyancy-dominated surface layer ($-z_i/L \to \infty$), the Monin–Obukhov length L is again no longer relevant and the shear-related scales u_* and T_* are dominated by the free convection scales $u_f(z)$ and $T_f(z)$. Thus the buoyancy-driven surface layer ($z \ll z_i$) is organized according to

$$\frac{f}{f_{\rm FC}} = A \approx O(1), \tag{3}$$

where $f_{\rm FC}$ is a scale formed from z, $u_f(z)$, and $T_f(z)$, and A is an order 1 constant. In a strict sense, free convection is characterized by $u_* \to 0$ and Q_0 is positive. Note, however, that in an unstable atmospheric surface layer the state represented by Eq. (3) may scale a statistic for $-z/L$ larger than some limiting value $-z_c/L$ in spite of u_* being finite. This was called ''local free convection'' by Wyngaard et al. (1971).

If buoyancy were to dominate shear in organizing surface layer statistics, then form (3) should describe the scaling. However, as pointed out by Wyngaard et al. (1971), because $u_*/u_f = (-z/L)^{-1/3}$ and $T_*/T_f = (-z/L)^{1/3}$, a normalized variable $f/f_{\rm FC}$ that scales on buoyancy-dominated motions according to form (3) can be rewritten in form (2). Thus, collapse onto form (2) is a necessary, but not a sufficient condition to conclude the dominance of shear-induced motions in the structure of a surface layer statistic (see also KB97).

Monin–Obukhov similarity, form (2), will result where surface layer influences are dominated statistically by local shear-induced structure characterised by scales z, u_*, and T_*. Other influences, for example, from the outer-scale buoyancy-driven motions (z_i, w_*, Θ_* scalings) or local buoyancy-driven motions (u_f, T_f scalings), must be negligible in comparison. As mentioned above, it is now well established that the horizontal motions near the ground scale on mixed layer scales z_i and w_* rather than on the local scales z and u_*, implying that z_i-scale buoyancy-driven motions are *directly* impressed on certain elements of surface layer structure. KB97 introduced the concept of ''indirect influence'' of outer-scale motions whereby the appropriate normalizing scale for f is the MO scale $f_{\rm MO}$, but that the functional dependence of $f/f_{\rm MO}$ retains an indirect influence of the boundary layer depth z_i through the stability parameter $-z_i/L$:

$$\frac{f}{f_{\rm MO}} = \Phi_f'\left(\frac{z}{L}, \frac{z_i}{L}\right) \approx O(1). \tag{4}$$

Conceptually, this modified statement of similarity implies that the shear-induced elements of the surface layer define *locally* the magnitude of f (in order-of-magnitude) while the depth of the boundary layer retains a *nonlocal* influence on the statistical structure of f.

Dimensional analysis implies that the similarity form (4) may be written equivalently as

$$\frac{f}{f_{\rm MO}} = \Phi_f''\left(\frac{z}{L}, \frac{z}{z_i}\right) \approx O(1) \quad \text{or} \tag{5}$$

$$\frac{f}{f_{\rm MO}} = \Phi_f'''\left(\frac{z}{z_i}, \frac{z_i}{L}\right) \approx O(1). \tag{6}$$

Whereas each form emphasizes different features of the structure of $f/f_{\rm MO}$, form (6) has the disadvantage that data that strictly satisfy MO scaling (2) will display a dependence on z_i/L when plotted as a function of z/z_i. Thus data should not be structured as per forms (5) and (6) without also applying form (4).

The KB97 analysis of LES data at $z_i/L = -0.44$, -3, and -8 indicated that, with the exception of horizontal velocity variance, f_{MO} is the appropriate order 1 scaling for all statistical variables when $z < -L$ and $z \ll -z_i$. However, the results suggested that form (4) was required for all near-ground velocity statistics, indicating that the boundary layer depth z_i has an indirect influence on the statistical structure of velocity in the surface layer. Temperature statistics, on the other hand, appeared to satisfy approximately MO scaling form (2), suggesting the dominance of local shear-generated motions in the structure of temperature in the absence of global outer-scale influence. However, consistent with Wyngaard et al. (1971) and Högström (1990), KB97 found that at convective states $z_i/L = -3$ and -8 the apparent MO scaling of temperature variance could be replaced by local free convection scaling form (3), suggesting the importance of buoyancy-driven motions in determining the structure of fluctuating temperature. Mean temperature, on the other hand, scaled as per MO similarity form (2).

b. The large-eddy simulations

The LESs were designed for unstable atmospheric boundary layers, statistically homogeneous in the horizontal and inhomogeneous in the vertical, over a horizontally homogeneous ground. The algorithmic details of the LESs were described in Khanna and Brasseur (1997). We summarize here the more important features of the LES relevant to the current study.

Because resolution near the ground is the limiting factor in LES studies of MO similarity, an ''embedded mesh'' algorithm was developed whereby an extrafine mesh of equivalent 256^3 nodes was placed in the lower 20% of the simulated atmospheric boundary layer, embedded within an overall 128^3 simulation spanning approximately $2z_i$ in the vertical, and either $5z_i \times 5z_i$ or $6z_i \times 6z_i$ in the horizontal. There simulations were applied to the MO analysis, a near-neutral case with $z_i/L = -0.44$ and $z_i = 525$ m, and two moderately convective cases with $z_i/L = -3$ and -8 and $z_i = 1060$ and 1020 m, respectively. In each calculation geostrophic mean wind was 15 m s^{-1} and Q_0 was varied from 0.01 to 0.24 K m s^{-1}.

The embedded mesh strategy was applied by KB97 to resolve as closely to the ground as possible. As pointed out in KB97, LES necessarily underresolves the horizontal integral scales of vertical velocity over roughly the first five grid levels, which, in the present simulations are at $z_r/z_i \approx 0.04$. Another issue of importance is the parameterization of the subgrid (SGS) terms in the dynamic equations. It is well known that the classical Smagorinsky closure overpredicts mean velocity and temperature gradients near the ground. It was found by KB97 that this overprediction is confined to the first few grid cells, while Juneja and Brasseur (1999) showed that the overprediction is a consequence of the model's poor handling of underresolution at the first few grid levels. KB97 carefully compared predictions using the single-equation Smagorinsky closure used by Moeng (1984) with a closure by Sullivan et al. (1994) designed specifically to overcome these overpredictions, and showed that the Sullivan et al. model dramatically improves the predictions of mean velocity and temperature gradients in the underresolved region, $z/z_i < 0.04$, when compared with the Kansas 1968 data reported in Businger et al. (1971). Thus, whereas the LES data in the underresolved region adjacent to the ground should be interpreted with caution, the region $z/z_i > 0.04$ is well suited to analysis of MO similarity.

The LES code, a modification of the Moeng and Sullivan et al. codes, applies pseudospectral in the horizontal and finite difference in the vertical. Consequently, periodic boundary conditions were applied in the horizontal over a horizontal domain, which resolved a minimum of 20 mixed layer integral scales of vertical velocity (Khanna and Brasseur 1998). Statistics were calculated by area and time averages as a function of height z. The boundary conditions in the vertical component of SGS stress and SGS flux vector were obtained, as with Moeng, using local drag laws, which relate surface values to resolved velocity at the first grid level.

The ground is modeled as a horizontally homogeneous flat rough surface with roughness height z_0. Surface temperature and surface stress $u_*^2 = (\overline{-u'w'})_0$ were evaluated using an iterative process, which assumed MO-similar profiles of mean temperature and velocity between the ground roughness height z_0 and first grid cell with forms given by Paulson (1970), restricting the simulations of roughness $z_0 \ll -L$ (Zilitinkevich et al. 1998). The roughness height z_0 was set at 0.01 m in the simulations. The lower boundary condition for pressure was derived using no slip at the ground, and at the upper boundary ($2z_i$) using a radiative condition involving the Brunt–Väisälä frequency. Turbulence variances are neglible above the capping inversion, so at the upper boundary subgrid stresses were set to zero while gradients in mean velocity were set to prescribed values.

3. Measurements and evaluation

The data used in this study are from the two field campaigns CFE1 (Concentrated Field Effort 1) and CFE2 of the NOPEX project, which were carried out during the summer of 1994 and 1995 in an area just north of Uppsala, Sweden (approximately 60°N and 17°E). Periods with simultaneous profile measurements, turbulence measurements, flight measurements, and radio soundings at the agricultural site Marsta have been selected.

The radio soundings were carried out with short time intervals: typically 4–5 radiosoundings per day, together with the airborne measurements (altogether 14 missions during 6 of the 14 days chosen for the analysis), they enable determination of how the height of the daytime

boundary layer evolved during the days used in this study.

a. The site Marsta

Marsta is located about 10 km north of Uppsala in the south of Sweden and is a typical agricultural site with scattered houses and trees. The ground is slightly rolling (at most approximately 5 m km^{-1}). In the sector 320°–20° there is a small forest about 700 m from the measuring tower that disturbs the measurements, so data with wind from this sector are rejected. There is a larger forest located 3 km to the east of the tower and another one located 5 km to the west. The area immediately surrounding the tower is a grass field, but only 20–40 m away the ground was covered by barley. Thus, for the wind sectors chosen for this analysis, the flux at the 10-m height originates primarily from the barley field.

b. Instrumentation

The tower at Marsta is 30 m high and has profile instruments at six levels: 0.84, 1.95, 4.78, 10.1, 17.2, and at 29.0 m, placed at the end of 1.5-m-long booms pointing into the direction 306°. Mean temperature was measured with Pt 500 sensors in ventilated radiation shields and mean humidity with the psychometric method, by combining data from ''dry'' and ''wet'' sensors. Mean wind speed and direction were measured with a combined cup anemometer and wind vane of in-house design. The measuring system is described in Lundin et al. (1990) and in Bergström and Lundin (1993).

At 10 m there was a Gill Solent 1012R2 ultrasonic anemometer (Gill Instrument, Symington, United Kingdom) for turbulence measurements. In order to correct for flow distortion, which is quite sizeable for this type of instrument, detailed wind tunnel calibration was carried out prior to installation on the tower. The calibration procedure is similar to that described in Grelle and Lindroth (1994), giving a matrix of calibration constants that correct for flow distortion. The sampling rate was 1 Hz for the slow response instruments and 21 Hz for the turbulence instrument. For the radio soundings Vaisala RS80 sondes were used, with an ascent rate of about 4 m s^{-1}, which gives a corresponding vertical resolution in the soundings of about 30 m.

Airborne measurements were made with an instrumented Sabreliner 40A twin jet aircraft. The speed of the aircraft was 100 m s^{-1} for all flights. Wind was measured with the gust radome probe technique (Brown et al. 1983) and air temperature with a standard Rosemount 102EAL total temperature probe. The aircraft used an inertial navigation system, Litton LTN-72, to define the horizontal velocity vector for the aircraft, the vertical acceleration, and the attitude angles relative to the earth. The instrumentation and evaluation of the measurements are described in Tjernström and Friehe (1991). Slant profiles were flown between lake Tämnaren, 30 km northwest of Marsta and Tisby, 40 km southwest of Marsta. The first profile during a flight started at lake Tämnaren at about 1500 m and ended at 100 m at Tisby. The second profile started at Tisby at 100 m and ended at about 1500 m at Tämnaren. Each slant profile was about 50 km long and had a duration of 10 min. In this paper profiles of sensible vertical heat flux and mean temperature profiles from the aircraft measurements were used to determine the depth of the boundary layer, z_i. No attempt was made to include airborne turbulence data directly into the similarity analysis.

The slant profiles were thus flown over an area situated 20–40 km from Marsta over relatively flat ground consisting of a mixture of agricultural and forest areas in about equal proportions. This differs from the Marsta site, which is entirely agricultural. Comparisons between BL height derived from the aircraft and from radio soundings carried out at the Marsta site show, however, no systematic differences.

c. The data

The crucial feature in this study is the boundary layer height. To be able to define this quantity, frequent radio soundings are needed in order to capture the development (growth) of the boundary layer. The dataset is reduced because of the necessity of having simultaneous radio soundings and profile and turbulence measurements, which were unfortunately not available for all days. For some of the days with radio soundings there are also flight measurements as discussed in the previous subsection.

Criteria for acceptance of data, other than completeness, were: (i) wind outside the sector with short fetch, 320°–20° and (ii) wind speed above 2 m s^{-1}. In this way data from 6 days in 1994 and 8 days from 1995 were finally selected for analysis. They include in all about 80 h. The number of radio soundings during these periods is 62 and the number of flights 14.

To determine the dimensionless wind gradient ϕ_m the wind gradient at 10 m is needed. Each 30-min wind profile was approximated by a second-order polynomial in lnz:

$$U = A \ln z + B(\ln z)^2 + C. \tag{7a}$$

Here A, B, and C were determined from the six wind measurements on the tower by the method of least squares. The wind gradient at 10 m is thus obtained after differentiation of Eq. (7):

$$\frac{\partial U}{\partial z} = \frac{A}{z} + 2B\,\frac{\ln z}{z}, \tag{7b}$$

with $z = 10$ m.

The gradient of potential temperature at 10 m was derived from the six temperature measurements on the tower in an exactly analogous manner, as was also the

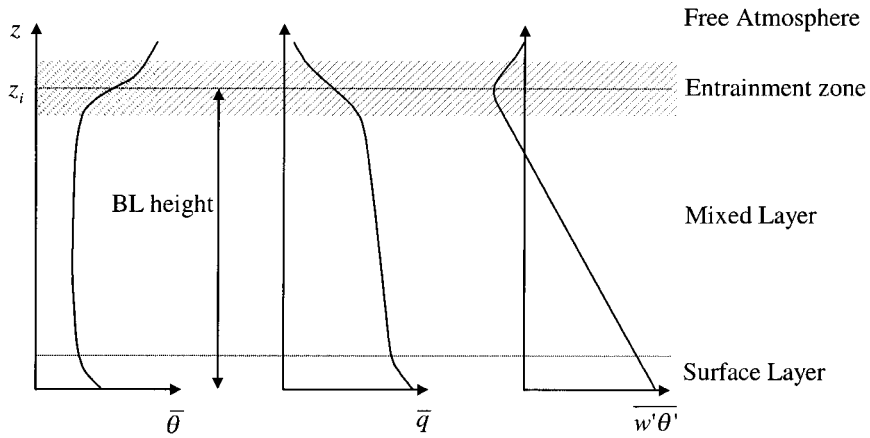

FIG. 3. Definition of boundary layer height in an idealized unstable atmosphere [after Stull (1988)]. Legend: $\overline{\theta}$ = mean potential temperature; $\overline{q}$ = mean specific humidity; $\overline{w'\theta'}$ = kinematic heat flux.

humidity gradient (used for buoyancy correction, cf. section 3e).

d. Determination of the height of the boundary layer

In the idealized atmosphere the height of the BL is typically described as the height of the first inversion in potential temperature or relative humidity, as illustrated in Fig. 3. This definition is roughly equivalent to the height of the minimum in vertical heat flux. Actual profiles, however, are often far from the ideal ones. Here the airborne measurements were very useful, giving the actual heat flux profiles and thus enabling direct determination of the height to the heat flux minimum, which is in agreement with the definition used in the LESs of KB97.

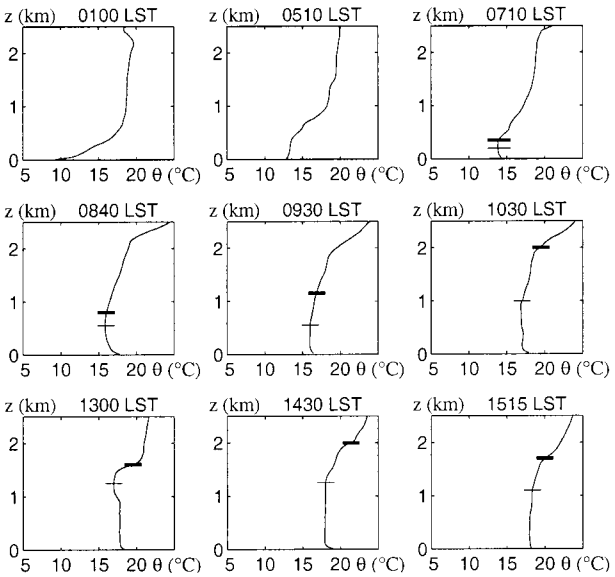

FIG. 4. Examples of consecutive temperature soundings (potential temperature) from one particular day, 3 Jul 1995. The thick horizontal line in each plot (upper line) denotes the approximate height of the heat flux minimum, which is equivalent to the definition of the boundary layer height, z_i in this paper. The thin line (lower line) indicates the corresponding approximate level where the heat flux changes sign.

Figure 4 shows examples of temperature profiles measured during one particular day, 3 July 1995, each curve representing an individual radio sounding. After the first establishment of a shallow mixed layer at 0710 LST, two heights are indicated in each plot as possible candidates for the BL heights, one lower, thin and one higher, thick line. The lower line corresponds approximately in each case to the height where there is a transition from slightly unstable or neutral to stable static stratification. The transition is also observed from airborne data to be the point where the heat flux changes sign. The upper line corresponds to the minimum in the heat flux and also, in most cases, to the point where there is a transition from slightly stable to stronger stratification. Roughly speaking, the thin line corresponds to the lower boundary of the entrainment zone and the thick line to its center. It is obvious from the graphs in Fig. 4 that the entrainment zone is sometimes very deep; note especially the sounding for 1030 LST. A reviewer suggested that the deep upper zone in these profiles might instead be due to presence of clouds. However, inspection of the corresponding humidity profiles rules out this possibility, the relative humidity being in the range 60%–80% and varying irregularly with both time and height.

For the times with airborne measurements the relevant BL height is simply taken as the height to the heat flux minimum. For the other times, the BL height is taken as the height to a point in the temperature curve where there is a change from slightly to very stable static stratification, in general agreement with the result from the airborne measurements.

The upper edge of the BL fluctuates, hence the radio soundings and the airborne measurements give only

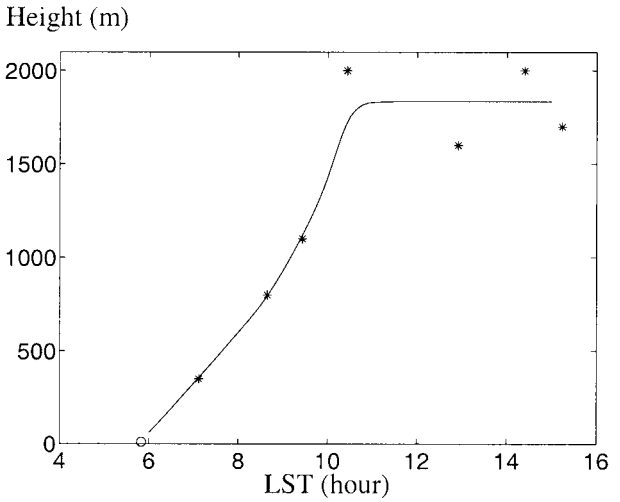

FIG. 5. Example of boundary layer height development during one particular day, 3 Jul 1995. The stars correspond to the horizontal thick lines in the various subplots of Fig. 4. The curve denoting the approximate mean development of the boundary layer height z_i has been drawn by eye.

snapshots of the height of the BL. To obtain a smooth development of the BL height during the day, an interpolation is done between the various BL heights obtained from the radio soundings, the flight measurements, and the tower measurement in the manners just described. The measurements on the 30-m-high tower capture the changes in stratification from stable to neutral to unstable, so that we know when the convective BL starts to develop.

Figure 5 shows, for the same day as in Fig. 4, the BL heights derived from the soundings and a smooth interpolation curve drawn by eye. The BL heights used in the calculations in this paper have all been taken from such interpolation curves. Of the 14 daily interpolation curves, 6 are backed up by two or three estimates based on airborne measurements, whereas the remaining 8 interpolation curves are based entirely on radiosoundings.

From the individual boundary layer height curves, like Fig. 5, it is possible to derive the time rate of change of the boundary layer height, dz_i/dt. This quantity is almost always an order of magnitude smaller than the corresponding convective mixed layer velocity scale (Deardorff 1970), $w_* = u_* k^{-1/3}(-z_i/L)^{1/3}$, so the surface layer is almost always in quasi-equilibrium as it grows. Specifically, on average for all 14 days, the ratio of w_* to dz_i/dt is about 20 during the morning period when the convective boundary layer is growing rapidly (cf. Fig. 5: the time period from 0600 to 1100 LST). The ratio is seldom below 10 even for single hours.

e. The turbulence data

To remove trends in the turbulence data, a 10-min running average was used in the evaluation of the measurements. In the analyses, 30-min averages were used for all variables. The MO length was calculated from the sonic data at the 10-m height on the tower from the following expression [a variation of Eq. (1)]:

$$L = -\frac{u_*^3 T_0}{kg(\overline{w'\theta_v'})_0}, \qquad (1')$$

where $u_* = \sqrt{\overline{(-u'w')}_0}$ and $\overline{(w'\theta_v')}_0$ is the flux of virtual potential temperature θ_v, which is obtained directly from evaluation of the sonic signals and the assumption is made that the measuring height 10 m is within the constant flux layer, so that the measured fluxes are good approximations of the corresponding fluxes at the surface. Although $\overline{(w'\theta_v')}_0$ is the correct quatity to enter Eq. (1′), the ordinary temperature flux $\overline{(w'\theta')}_0 = Q_0$ is needed in $T_* = Q_0/u_*$.

According to Lumley and Panofsky (1964), the following relation is valid to good approximation:

$$\overline{(w'\theta')}_0 = \frac{\overline{(w'\theta_v')}_0}{\left(1 + \frac{0.07}{\beta}\right)}, \qquad (8)$$

where $\beta = H/E\lambda$ = the Bowen ratio, with $H = \rho c_p Q_0$ = the flux of sensible heat from the groud, and $E\lambda$ = the turbulent flux of latent heat, λ being the latent heat of vaporization.

Bowen ratio values were derived from the simultaneous gradient of potential temperature and humidity, with the assumption that the exchange coefficients for heat and humidity are equal:

$$\beta = \left(c_p \frac{\partial \Theta}{\partial z} \Big/ \frac{\partial q}{\partial z}\lambda\right),$$

where q is the mixing ratio (kg H_2O/kg air).

In dry climates the Bowen ratio is often large, so that the correction (8) is usually of order 10% or less. In the present experiment the crop, however, was growing profusely, so that β was regularly considerably below unity. This gives a mean value for the correction of around 18%, with progressively larger percentage error for decreasing values of $\overline{(w'\theta_v')}_0$. Thus, the correction (8) and the use of virtual potential temperature in Eq. (1′) is vital for obtaining unbiased results in this study. Plots of ϕ_h and of σ_T^2/T_*^2 against z/L with and without these corrections (not shown here) vividly illustrate this point.

f. Data quality and measurement uncertainties

Validation of predictions from MO similarity theory requires accurate measurements of mean profiles and moments in a constant flux layer in approximate equilibrium. In order to get such conditions, a flat upwind area with uniform surface conditions covering the ''flux footprint'' of the entire surface layer is needed. The tower site Marsta fulfils this requirement for the wind directions selected for this study, with flat and uniform

barley fields extending for more than a kilometer in the upwind direction.

In order to distinguish discrepancies from MO theory predictions, requirements on measurement quality are high. As mentioned above, the sonic anemometer was calibrated in a large wind tunnel prior to the experiment, which resulted in a matrix that enabled very accurate correction for flow distortion from the instrument itself to be executed on each individual data scan. As a result, instrumental inaccuracies in derived fluxes and other second-order moments are negligibly small. Nevertheless a random component exists that can reflect not only natural nonlinear dynamics, but also variability in the boundary or initial conditions. With the averaging time 30 min, this random error was estimated to ±16% for the momentum flux and ±10% for the sensible heat flux by Dyer et al. (1982). It is possible that the error is appreciably greater for parameters, which are influenced by boundary-layer scale fluctuations, compare with in particular the analysis for the dimensionless wind gradient ϕ_m below. In deriving this quantity, as well as the corresponding dimensionless temperature gradient ϕ_h, the accuracy estimating the corresponding wind and potential temperature gradients, $\partial U/\partial z$ and $\partial\Theta/\partial z$, is also essential. As shown in the appendix, the method employed here [based on Eq. (7b)] has an uncertainty of less than 10% for both the wind and the temperature gradients.

The accuracy in the estimation of the boundary layer height z_i is crucial to this study. It can be argued that individual radiosoundings and airborne measurements will give only snapshots of a highly variable quantity. This is of course true, but we estimate the relative error to be only of order ±10%, which is more than acceptable in the present context. Figure 5 illustrates our argument. Here a curve has been fitted by eye as an approximation to the 8 measurements of z_i available for this particular day. During the time period between 1000 LST and 1600 LST there are four data points that clearly indicate that z_i has reached a constant mean value. The scatter of these four points around the line is c. ±200 m, which is ±10% of the mean value. The smooth rise of the curve from 0600 LST to around 1000 LST is an indication that the relative scatter of the other measurements is unlikely to be larger. All estimates of z_i used in this study are derived from interpolation curves obtained in this manner.

4. Analysis of the data

a. Statistics including velocity

1) NONDIMENSIONAL WIND GRADIENT

According to the MO theory, MO-normalized wind gradient should be a function only of the stability parameter z/L:

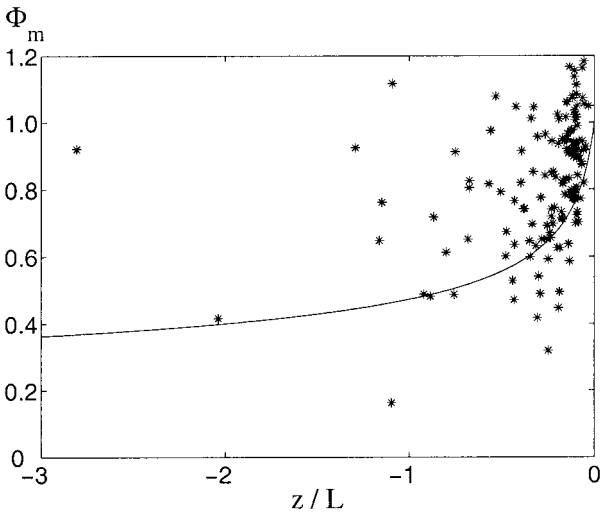

FIG. 6. Plot of ϕ_m against z/L for all measurements in this study [solid line from Högström (1996)].

$$\frac{kz}{u_*}\frac{\partial U}{\partial z} = \phi_m(z/L).$$

As already noted in the introduction, however, there is considerable scatter among the various experimental measurements of ϕ_m (Fig. 1). Figure 6 is a plot of all the ϕ_m measurements from the present study. Also drawn is the curve for the expression suggested by Högström (1996). The data are seen to have a high degree of scatter. According to the LES simulations of KB97, ϕ_m is expected to be a function of both z/L and z_i/L.

To facilitate distinguishing possible influences of z_i/L, the data have been grouped into the following widely separated stability ranges: $-0.5 > z_i/L > -5$, $-25 > z_i/L > -35$, and $z_i/L < -60$. For clarity of presentation, data points in the z_i/L ranges between the ranges selected for analysis are not included, so subsequent plots contain much fewer data points than Fig. 6. The new subsets have been plotted against z/L in Fig. 7, using different symbols for data from each of the three z_i/L groups (see figure legend for specification). Although there is considerable scatter among the data in each stability group, there is a significant and very clear ordering of the three datasets, with the least unstable data to the right in the figure. Furthermore, the three sets of data remain separated at small $-z/L$. This general trend is in agreement with a corresponding plot in KB97 from the LES simulations, which is overlaid in Fig. 7 with the short double line representing $z_i/L = -0.44$, the dashed line $z_i/L = -3.0$, the dotted line $z_i/L = -8.0$. Note that the LES data are over a much narrower z_i/L range than the experiment.

2) HORIZONTAL VELOCITY VARIANCE

Earlier studies, by, for example, Panofsky et al. (1977) and Deardorff (1972), have shown that the hor-

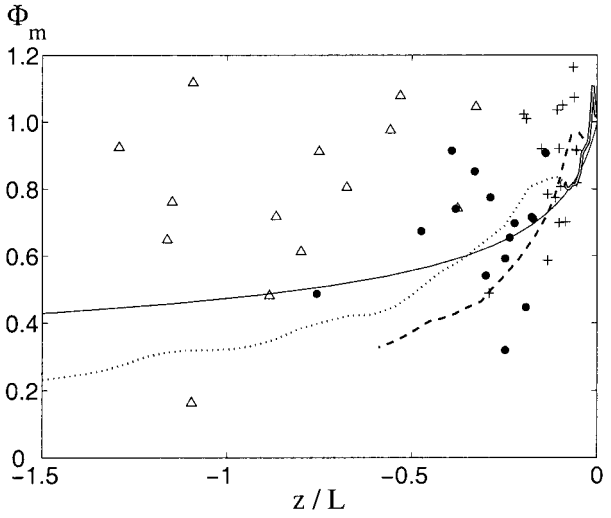

FIG. 7. Plot of ϕ_m against z/L for measurements in three z_i/L ranges: pluses, $-0.5 > z_i/L > -5$, filled circles, $-25 > z_i/L > -35$, and triangles, $z_i/L < -60$. The thin line is from Högström (1996). The other three lines are from the LES of KB97: double line, $z_i/L = -0.44$; dashed line, $z_i/L = -3$; dotted line, $z_i/L = -8$.

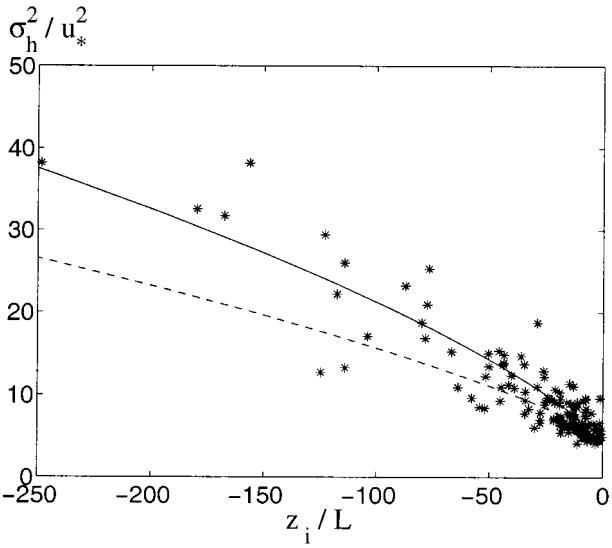

FIG. 8. Plot of σ_h^2/u_*^2 against z_i/L. The solid line is a curve fit to the measurements, Eq. (11). The dashed line is from Panofsky et al. (1977), our Eq. (9).

izontal standard deviation of velocity depends strongly on z_i/L. Panofsky et al. (1977) found that their measurements could be represented by the following expression:

$$\frac{\sigma_h^2}{u_*^2} = (12 + 0.5z_i/-L)^{2/3}, \tag{9}$$

where

$$\sigma_h^2 = \frac{\overline{u'^2} + \overline{v'^2}}{2}.$$

Data of σ_h^2/u_*^2 from the present experiment have been plotted against z_i/L in Fig. 8. For relatively small values of $-z_i/L$ the trend of the present data is in general agreement with Eq. (9), which is represented by the broken curve in the figure. But for $z_i/L \leq -50$, Eq. (9) systematically underpredicts σ_h^2/u_*^2. Figure 8 shows that u_* is not the correct normalization scale for horizontal velocity variance, suggesting a strong influence from mixed layer eddies on horizontal motions in the surface layer. We therefore rewrite Eq. (9) using the mixed layer velocity scale w_*:

$$\left(\frac{\sigma_h}{w_*}\right)^2 = k^{2/3}\left(\frac{12}{-z_i/L} + 0.5\right)^{2/3}. \tag{10}$$

From this relation we have for $z_i/L \ll -24$ and with the von Kármán constant $k = 0.4$:

$$(\sigma_h/w_*)^2 \approx \text{const} = \alpha_h = 0.34 \qquad (z_i/L \ll -24).$$

In Fig. 9, $(\sigma_h/w_*)^2$ has been plotted against z_i/L. It is seen that, except in near-neutral conditions, $-z_i/L \ll 1$, w_* is the appropriate scale for horizontal velocity variance. Furthermore, $(\sigma_h/w_*)^2$ is roughly constant for $z_i/L \leq -40$, with a value close to 0.5, rather than 0.34 as obtained by Panofsky et al. (1977). This is in good agreement with Willis and Deardorff (1974), who measured $\alpha_h \approx 0.5$ in the surface layer. A very good overall fit to the data, the full line in Fig. 9 is obtained by adjusting (10) to read:

$$\left(\frac{\sigma_h}{w_*}\right)^2 = k^{2/3}\left(\frac{10}{-z_i/L} + 0.88\right)^{2/3}. \tag{11}$$

This expression has been plotted as a solid line in Fig.

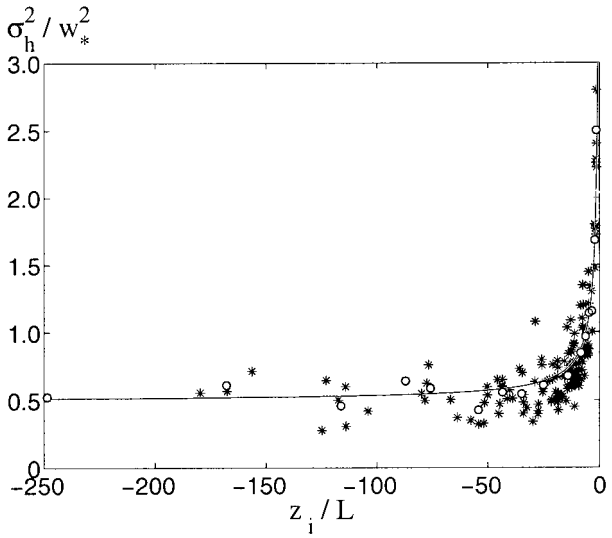

FIG. 9. Horizontal velocity variance normalized by w_*^2, against z_i/L. Stars are individual measurements, open circles are mean values over finite z_i/L ranges. For $z_i/L < -40$, $\sigma_h^2/w_*^2 \approx$ constant $= \alpha_h \approx 0.5$. The thin curve is Eq. (11).

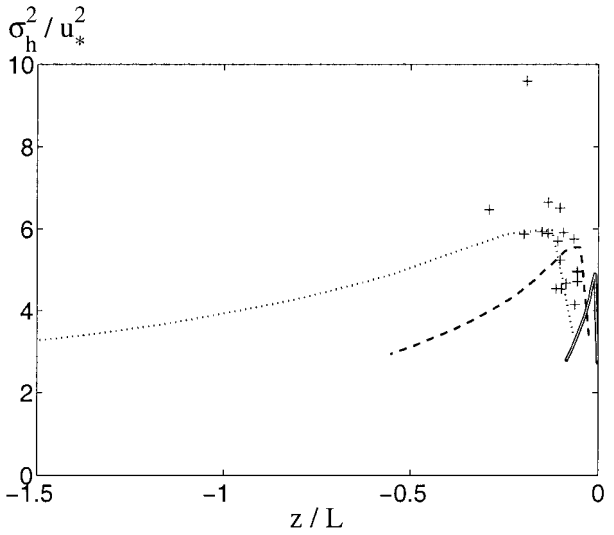

FIG. 10. Horizontal velocity variance normalized by u_*^2, against z/L. The pluses are measurements representing the least unstable data group, $-0.5 > z_i/L > -5$. The curves are from the LES of KB97: double line, $z_i/L = -0.44$; dashed line, $z_i/L = -3$; dotted line, $z_i/L = -8$.

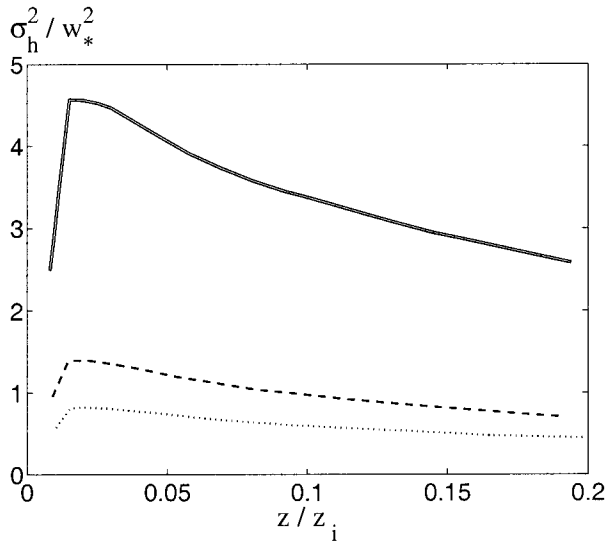

FIG. 11. Plot of σ_h^2/w_*^2 against z/z_i from KB97: dotted curve, $z_i/L = -8$; dashed curve, $z_i/L = -3$; double curve, $z_i/L = -0.44$.

9. It is seen to fit the bin averages (the open circles) closely.

Figure 10 is a plot of $(\sigma_h/u_*)^2$ against z/L for the least unstable data group, $-0.5 > z_i/L > -5$, to be compared with the LES of KB97 for $z_i/L = -0.44$, -3, and -8, shown as the three curves. Except for one outlier, the measurements appear to follow the general trend of the LES curves in that the (shear) normalized variance grows with $-z/L$ to what appears to be a plateau near $z/L \approx -0.15$. The corresponding data points at higher convectively unstable states, $-25 > z_i/L > -35$ and $z_i/L < -60$ (not included in Fig. 10), exhibit large scatter but increase generally with increasingly negative z/L to values in the range 30–40 for $z/L = -2$, consistent with a progressively dominating influence of buoyancy-driven motions on horizontal velocity variance near the ground.

Figure 11 shows the LES of $(\sigma_h^2/w_*)^2$ for the three stabilities $z_i/L = -0.44$, -3, and -8, respectively, plotted against z/z_i. Figures 10 and 11 indicate only moderate variation of $(\sigma_h/w_*)^2$ with height in the surface layer (say $z/z_i < 0.1$) but strong variation with z_i/L (i.e., variation in mean magnitude between the three curves). This variation is compared with the corresponding experimental results in Fig. 12, the bars indicating the ranges of σ_h^2/w_*^2 taken from Fig. 11 for each of the three z_i/L-curves. Here the Δ symbols are the maxima in the curves of Fig. 11 ($z/z_i \approx 0.02$–0.03) and the bars give the variation in $(\sigma_h/w_*)^2$ to $z/z_i \approx 0.1$. The LES results follow the trend of the experimental data very well. Note that the experimental results, having z/z_i values mostly in the range 0.01–0.03, correspond closely to the upper limit of the bars. Note also that the variation in normalized variance between the near-ground and z/z_i of 0.1 (the length of the bars) decreases with decreasing z_i/L, indicating the increasing influence of the buoyancy-driven outer scales on the near-wall region. The particularly large jump in variation between the moderately convective state $z_i/L = -3$ and the near-neutral state $z_i/L = -0.44$ reflects a disappearance of outer buoyancy-driven motions in near-wall structure in the near-neutral limit.

From Figs. 9 and 12 it is clear that w_* is the proper

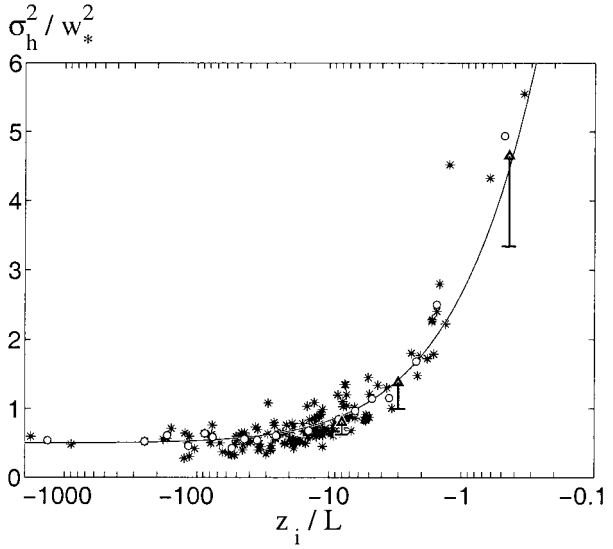

FIG. 12. Horizontal velocity variance normalized by w_*^2, against $-z_i/L$. The stars are individual measurements, the open circles are mean values over finite z_i/L ranges, and the solid curve is Eq. (11). The vertical lines are from the LES results of KB97. The symbol Δ is maximum σ_h^2/w_*^2 from Fig. 11, at $z/z_i \approx 0.02$–0.03, while the bars give the range of normalized variance from near the surface to $z/z_i = 0.1$.

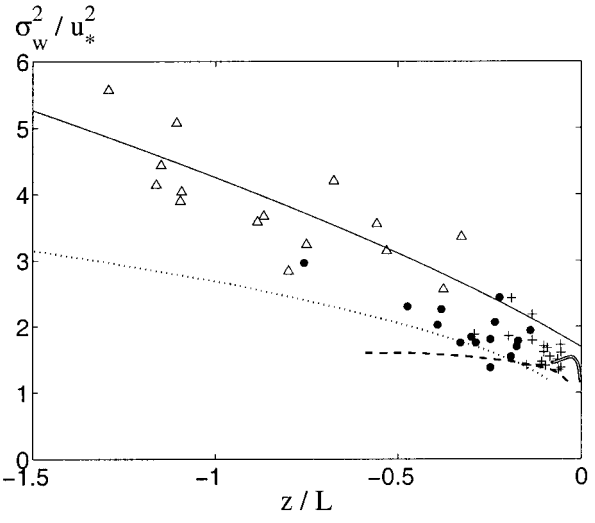

FIG. 13. Plot of σ_w^2/u_*^2 as a function of z/L. The measurements are divided according to stability: plus, $-0.5 > z_i/L > -5$; filled circles, $-25 > z_i/L > -35$; triangles, $z_i/L < -60$. The thin solid line is the expression from Panofsky et al. (1977), our Eq. (12). The remaining curves are from the LES of KB97: double line, $z_i/L = -0.44$; dashed line, $z_i/L = -3$; dotted line: $z_i/L = -8$.

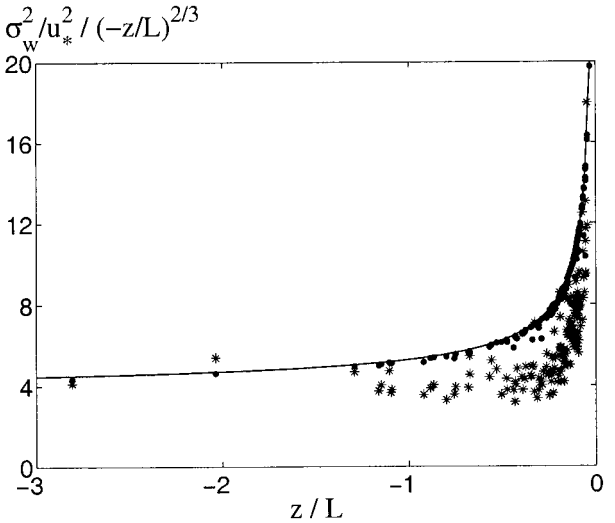

FIG. 14. Plot of $\sigma_w^2/u_*^2/(-z/L)^{2/3}$ against z/L. Stars are obtained from measurements of the normalized vertical velocity variance. Small black dots have been derived with Eq. (13) using values of z/L and z/z_i from the same measurements. The curve is obtained from Eq. (13) in the limit $z/z_i \to 0$.

scaling velocity for σ_h over most of the z_i/L-range, $-z_i/L \geq 1$, u_* being the dominant scale when $-z_i/L \leq 0.5$, and both are relevant scales when $1 \geq -z_i/L \geq 0.5$.

3) VERTICAL VELOCITY VARIANCE

Panofsky et al. (1977) concluded that $(\sigma_w/u_*)^2$ is a function of z/L only. In Fig. 13 their relation (the thin solid line)

$$\left(\frac{\sigma_w}{u_*}\right)^2 = 1.69(1 - 3z/L)^{2/3} \tag{12}$$

has been plotted together with the LES simulations of KB97 and the experimental data, divided into three z_i/L groups. For $-z/L \geq 0.5$, the experimental data follow Eq. (12) without bias. For smaller $-z/L$-values, both the experimental data and the LES curves are generally below the curve representing Eq. (12). The experimental data in the range $-0.5 > z_i/L > -5$ (pluses) follow the mean trend of the LES curves for $z_i/L = -0.44$ and -3.0 for $z/L > -0.3$ but deviate for more negative z/L. Whereas the trends in the LES curves follow qualitatively the data, overall the LES predictions of $(\sigma_w/u_*)^2$ are too low. The explanation for the overall underprediction of vertical velocity variance by LES is unclear, however this may reflect spurious damping introduced near the surface by a combination of the drag law model in the boundary conditions for SGS stress [which assumes a constant surface exchange coefficient, see Wyngaard et al. (1998)], and a reduction in fluctuations inherent in the Sullivan et al. (1994) SGS model used in the simulations to improve predictions of mean shear (section 2b).

A relation that includes the boundary layer height was obtained by Peltier et al. (1996) from a generic model of horizontal spectrum of vertical velocity:

$$\frac{\sigma_w^2}{u_*^2} = 1.6 + \left(-\frac{z}{L}\right)^{2/3}\left[3.7 - 46\left(\frac{z}{z_i}\right)^{4/3}\right]. \tag{13a}$$

Our data is calculated when z/z_i is of order 0.01 for all but a few early morning cases, so that the second term in the brackets of Eq. (13) is generally negligible. For $-z/L \gg 0.3$, Eq. (13) gives the local free convection limit:

$$\frac{\sigma_w^2}{u_*^2} \approx 3.7(-z/L)^{2/3}, \tag{13b}$$

which is close to the Panofsky et al. Eq. (12) in the same limit.

In Fig. 14 $(\sigma_w/u_*)^2/(-z/L)^{2/3}$ is plotted against z/L together with Eq. (13) at $z/z_i \ll 1$. We find that when $z/L \leq -0.3(\sigma_w/u_*)^2 \propto (-z/L)^{2/3}$ with a proportionality constant of about 4, that is, slightly larger than that predicted by Eqs. (13b) and (12). Thus, in the limit of local free convection, the present data support Eq. (13a) near the ground. However, the figure shows that Eq. (13a) asymptotes to Eq. (13b) at much lower z/L and that Eq. (13a) generally overpredicts the data at intermediate z/L.

In Peltier et al. (1996) the assumption is made that σ_w^2/u_*^2 is independent of z near the ground in near-neutral conditions in the limit $-z_i/L$ and $-z/L$ approaching zero [Eq. (13a)]. In contrast to this traditional view, Högström (1990) proposed the following relation for the near-neutral boundary layer near the ground:

$$\sigma_w/u_* = 0.12 \ln(zf_c/u_*) + 1.99, \tag{14}$$

where f_c = the Coriolis parameter. This unexpected finding was explained by Högström (1990) to result from ''inactive'' turbulence where, in analogy with laboratory findings of turbulent boundary layer flow in a nonzero-pressure-gradient flow (Yaglom 1979), a mean ''pressure gradient length scale'' characterized vertical velocity variance near the ground under near-neutral conditions:

$$\delta_p = u_*^2 \left(\frac{1}{\rho} \frac{\partial P}{\partial x} \right)^{-1}. \tag{15}$$

In the atmosphere $(1/\rho)(\partial P/\partial x) = f_c G \sin\alpha$ and

$$\delta_p = \frac{u_*^2}{f_c G \sin\alpha}, \tag{16}$$

where G is the magnitude of the geostrophic wind and α is the cross-isobaric angle at the earth's surface. Neutral similarity theory (e.g., Tennekes 1982) implies that sin α is proportional to u_*/G, so that finally

$$\delta_p = C \frac{u_*}{f_c}, \tag{17}$$

where C is a constant ≈ 0.08. With numerous measurements of σ_w/u_* from 3, 6, and 13 m in the stability range $-0.1 \le z/L \le 0.1$, it was shown by Högström (1990) that Eq. (14) gives a very good representation of the data (with $\alpha = 60°$, $f_c = 1.26 \cdot 10^{-4}$). Later, Smedman (1991) verified this relation with measurements during near-neutral conditions at other field sites in Sweden.

From an analysis of spectra of vertical velocity in near-neutral conditions Högström (1990) showed that the observed increase of vertical velocity variance with height was entirely due to a corresponding increase in the low-frequency spectral range with height. This was interpreted as evidence for large-scale, inactive turbulence, analogous to what was observed in shear-driven laboratory nonzero pressure gradient boundary layers (Bradshaw 1967). The observed increase in vertical velocity variance with height is also in agreement with the idea of Hunt (1984) and Hunt et al. (1988), who represent the velocity field near the ground as the sum of velocity field from an hypothetical eddy in the absence of a ground surface and its ''image.'' The implication is that the vertical velocity field associated with the largest scales is strongly suppressed near the ground and vertical velocity variance gradually increases with height, as observed.

The values of σ_w/u_* for cases with $z/L > -0.2$ ($z_i/L \ge -20$) from the present experiment were regressed against $\ln(zf_c/u_*)$, giving a slope of 0.11 and an intercept of 1.96, in close agreement with the expression obtained by Högström (1990), reproduced here as Eq. (14). Figure 15 shows σ_w^2/u_*^2 plotted as a function of $\ln(zf_c/u_*)$, the black dots representing the cases with $-z/L < 0.2$ ($z_i/L \ge -20$). Also drawn is the curve representing the square of the right-hand side of Eq. (14); that is,

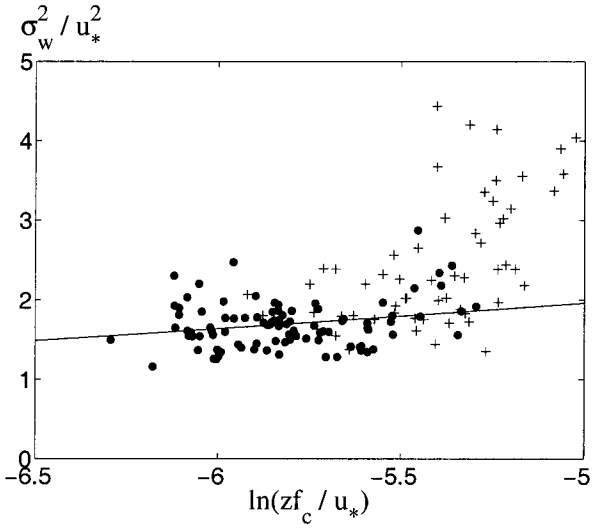

FIG. 15. Plot of σ_w^2/u_*^2 against $\ln(zf_c/u_*)$, where f_c is the Coriolis parameter. The filled circles are data with $-z/L \le 0.2$ and the pluses data with $-z/L > 0.2$. The curve drawn is Eq. (18a), which is the square of the regression expression for σ_w/u_* against $\ln(zf_c/u_*)$. Note, that the data used in the regression correspond to the black dots only in the present plot (i.e., the pluses are not included).

$$(\sigma_w/u_*)^2 = 4.0 + 0.0144(\ln zf_c/u_*)^2 + 0.48 \ln zf_c/u_*, \quad -z/L \le 0.2 \tag{18a}$$

As mentioned above, relation (14) was tested on data in the stability range $-0.1 \le z/L \le 0.1$ by Högström (1990). Although Högström (1990) specifically tested Eq. (14) in that range, Fig. 17 in that paper suggests that the relationship may apply at $z/L < -0.2$, as indicated by Fig. 15.

The above results suggest replacing Eq. (13) by a combination of equations, consisting of the square of Eq. (14) for $z/L \ge -0.2$, and a modified form of Eq. (13) for $z/L < -0.2$. A very good overall fit is obtained for:

$$(\sigma_w/u_*)^2 = 4.0 + 0.0144(\ln zf_c/u_*)^2 + 0.48 \ln zf_c/u_*, \quad -z/L \le 0.2, \quad -z_i/L \le 20 \tag{18b}$$

$$= 0.6 + (-z/L)^{2/3}[3.44 - 46(z/z_i)^{4/3}] \text{ other.} \tag{18c}$$

Calculations show that for the entire dataset ($N = 156$), which covers the range $0 > z/L > -20$, the mean of the difference is 0.07 and the standard deviation 0.42.

b. Statistics including temperature

1) MEAN TEMPERATURE GRADIENT

For MO-scaled temperature gradient, the prediction from the MO theory is

$$\frac{kz}{T_*} \frac{\partial \Theta}{\partial z} = \phi_h(z/L), \tag{19}$$

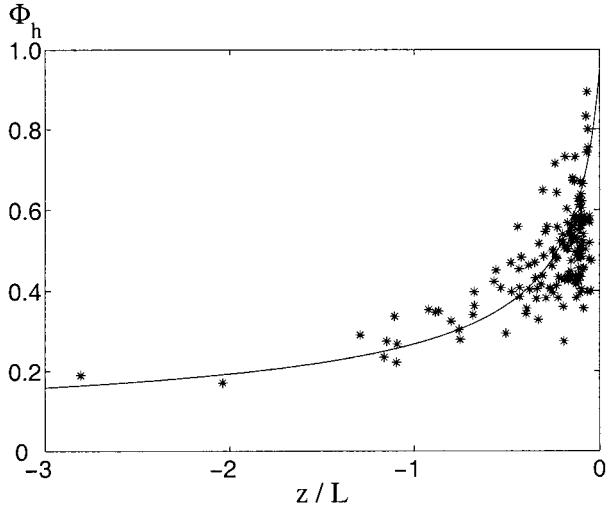

FIG. 16. Plot of ϕ_h against z/L for all measurements in this study [Solid line from Högström (1996)].

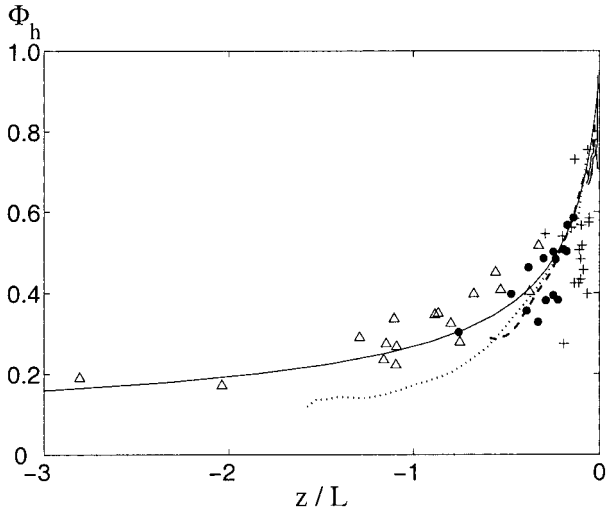

FIG. 17. Plot of ϕ_h against z/L. The measurements pluses, $-0.5 > z_i/L > -5$; filled circles, $-25 > z_i/L > -35$; and triangles, $z_i/L < -60$. The thin solid line is from Högström (1996). The remaining curves from the LES study of KB97: double line, $z_i/L = -0.44$; dashed line, $z_i/L = -3$; dotted line, $z_i/L = -8$.

where $T_* = -Q_0/u_*$ is a temperature scale associated with shear-induced motions and Θ the mean potential temperature.

As noted in the introduction, data of ϕ_h from most field experiments appear to collapse better than corresponding ϕ_m (data cf. Figs. 1 and 2). This observation is in agreement with the LES results of KB97, who observed no significant dependence of ϕ_h on z_i/L.

Figure 16 shows ϕ_h plotted against z/L from the present experiment, together with the expression recommended by Högström (1996), while in Fig. 17 the data have been subdivided in z_i/L groups as was done for ϕ_m in Fig. 7. Comparing ϕ_m in Fig. 7, with ϕ_h in Fig. 17, the much lower level of scatter for ϕ_h is immediately apparent. A slight ordering with z_i/L, although less clear than for ϕ_m in Fig. 7, suggests that there may be a tendency for the most unstable data (triangles) to cluster above Högström's mean curve and the least unstable group (pluses) in a band somewhat below the curve. The intermediate stability group (black dots) appears to lie between and overlap the other two groups. The LES curves from KB97 shown in Fig. 17 also suggest a slight tendency for the curves to order according to z_i/L similar to the observations, but over a narrow range of stabilities.

2) TEMPERATURE VARIANCE

Figure 18 shows MO-scaled temperature variance σ_T^2/T_*^2 near the ground ($z \ll z_i$), plotted against z/L with the data divided into three z_i/L groups in the manner of Fig. 17. Also drawn is a line corresponding to the free convection prediction $\sigma_T^2/T_*^2 = 0.9\ (-z/L)^{-2/3}$, where 0.9 was found by Wyngaard, et al. (1971) and Högström (1990) and as well as by KB97 using LES.

The thin curve on Fig. 18 is equivalent to $\sigma_T^2/T_f^2 = 0.9 \sim O(1)$ so that, as discussed in section 2a, a collapse onto this curve implies the dominance of buoyancy-driven motions in organizing the structure of temperature variance. The intermediate stability state data (filled circles, $z_i/L \sim -25$ to -35) and the moderately convective LES data ($z_i/L = -8$ and -3) appear to follow local free convection to $-z/L$ much less than 1. Furthermore, whereas T_f maintains order 1 scaling in the limit $-z/L \to 0$, the MO scale T_* fails to normalize temperature variance in this limit. We conclude that

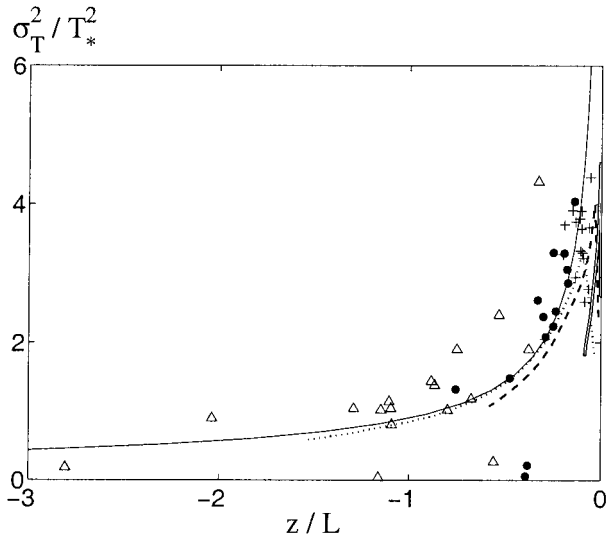

FIG. 18. Plot of σ_T^2/T_*^2 against z/L for measurements in the three z_i/L ranges: pluses, $-0.5 > z_i/L > -5$; filled circles, $-25 > z_i/L > -35$; triangles, $z_i/L < -60$. The thin solid line is the expression for local free convection: $\sigma_T^2/T_*^2 = 0.9(-z/L)^{-2/3}$, which corresponds to $\sigma_T^2/T_f^2 = 0.9$. The remaining curves are LES data of KB97: double line, $z_i/L = -0.44$; dashed line, $z_i/L = -3$; dotted line, $z_i/L = -8$.

buoyancy-driven motions characterize temperature variance structure in the near-wall region when buoyancy forces are globally significant (presumably when $-z_i/L > 1$). Less surprising is the dominance of buoyancy motions in scaling temperature variance in the near-ground region when $-z/L > 1$, as is apparent with the most unstable group in Fig. 18 (triangles, $z_i/L < -60$).

Deviations from the local free convection curve should be anticipated in the neutral limit $-z_i/L \to 0$, since in this limit buoyancy plays no role in the dynamics and the shear scale T_* should become the appropriate normalization. The LES curve for $-z_i/L = -0.44$ (double curve) shows clear departure from local free convection scaling, and the least unstable group ($z_i/L \sim -0.5$ to -5, pluses) suggests a clustering of data toward the near-neutral LES. Taking experimental and LES data together, in the near-neutral limit temperature variance appears to scale as $\sigma_T^2/T_*^2 \sim 4$ as $-z/L \to 0$ while σ_T^2/T_f^2 becomes very large and clearly departs from order 1 scaling.

We conclude that in the moderately convective boundary layer, temperature variance near the ground is organized by the buoyancy scale T_f while mean temperature gradient is organized by the shear scale T_*. In the neutral limit, however, T_f is replaced to T_* as the relevant scale for temperature variance near the ground.

5. Discussion and conclusions

Comparisons have been made between LES data of the slightly unstable and near-neutral atmospheric surface layer by Khanna and Brasseur (1997) and corresponding field data from two intensive summertime field campaigns in Sweden. The field data include turbulence measurements at one level close to the ground (10 m), slow response ''profile'' measurements at six levels in the lowest 30 m and, most importantly, aircraft measurements and radio soundings that enable (with the aid of a proper interpolation scheme) accurate determination of the depth of the atmospheric boundary layer at all times. In all about 160 30-min samples have been selected for analysis for stability conditions over a very wide range of z_i/L, from -0.3 to -1800, which result from combining convective boundary layer depths z_i from about 100 to 2000 m and Monin-Obukhov length L from about -0.5 to -350 m. The relatively wide range of z_i is obtained by including values not only from the afternoon equilibrium phase but also from several hours before noon for each of the 14 days used in the analysis. By comparing the rate of growth of the convective boundary layer with the convective velocity scale w_*, it was shown that the surface layer is in quasi-equilibrium even prenoon.

In contrast with the experimental data at one height $z \ll z_i$, and many stability states, the LES data of KB97 include all heights z throughout the boundary layer (where $z/z_i < 0.04$ must be treated with some caution), but only three stability states. Thus the LES were not restricted to the near-ground region $z \ll z_i$, but were restricted to the three z_i/L, -0.44, -3.0, -8.0. Furthermore, the boundary layer state was well controlled with the LES and statistical sample was excellent. Consequently the LES and experimental data should be viewed as complementary.

Based on their analysis of LES for two convective and one near-neutral boundary layer, Khanna and Brasseur (1998) made the following concluding statement: ''Our analysis, therefore, suggests a stronger coupling between the inner and outer regions of the boundary layer than previously realized.'' This statement was strongly supported by the current analysis, which combined field measurements with the LES data for a closer examination. We conclude the following.

(i) The nondimensional wind gradient, ϕ_m, shows clear ordering of the data with the stability parameter z_i/L in addition to the expected dependence on z/L. The trend of the field data is in general agreement with that of the LES and extends the result to much higher $-z_i/L$.

(ii) In agreement with KB97, the horizontal velocity variance, σ_h^2 is found to scale with the convective velocity scale, w_*, over most of the z_i/L-range, u_* being the relevant scale only for the near-neutral case (roughly $z_i/L > -1$). This result is in agreement also with Khanna and Brasseur (1998).

(iii) For the vertical velocity variance, σ_w^2, KB97 find only relatively little dependence on z_i in the region $z \ll z_i$ and $z \ll -L$ near the ground in the shear-dominated layer. This might be explained by the ''image model'' of Hunt (1984) and Hunt et al. (1988), in which vertical velocity associated with the largest eddies are damped near the surface. Thus, the proper velocity scale for σ_w is u_*, and σ_w^2/u_*^2 is found to be dependent on z/L for $-z/L \geq 0.2$. For $-z/L \leq 0.2$ (and $-z_i/L \leq 20$) σ_w^2/u_*^2 is found to scale with z/δ_p, where δ_p is the mean pressure gradient length scale proportional to u_*/f_c, where f_c is the Coriolis parameter. Regression gives effectively the same relation as that obtained by Högström (1990) for the stability range $0.1 > z/L > -0.1$, a result previously interpreted as a reflection of large, so-called inactive motions. Here σ_w/u_* is found to increase with the logarithm of z/δ_p. Close to the ground σ_w/u_* approaches 1.0, the value obtained for flat plate nonzero pressure gradient boundary layer, which is known to contain no inactive turbulence (Bradshaw 1967). It is thus in agreement with the image theory of Hunt (1984) that big eddies contribute to a vertical velocity variance that increases slowly with height in the surface layer. Note that the big eddies that characterize the near-neutral regime scale with $\delta_p > z_i$ and not with z_i, so they are likely governed by the shear instability of the boundary layer, possibly in conjunction with breaking gravity waves of the same scale, which are simultaneously present in the stably stratified free atmosphere immediately above the BL (cf. Högström et al. 1999). Although the concept was formulated for the shear-driven boundary layer, a scaling on z/δ_p without

dependence on z/L appears to work in the shear-dominated region of moderately convective boundary layers (Fig. 15), although the reason for this is not clear.

(iv) The nondimensional temperature gradient, ϕ_h, shows a slight ordering with z_i/L, but the variation with z_i/L is much less than for ϕ_m. KB97 concluded that the influence of stability state on mean temperature gradient was insignificant, however close examination of their results suggest a slight trend as indicated by the measurements, but over a narrower range of z_i/L.

(v) The variance of temperature fluctuations was found to scale on T_f^2, except in the neutral limit when buoyancy force is negligible and T_* is the appropriate scale near the ground. These characteristics observed in the LES of KB97 were generally confirmed by the experimental data.

The temperature statistics summarized under (iv) and (v) are conveniently discussed together with reference to KB97. In summary, (i) $d\Theta/dz$ scales on T_*/z so long as $-z_i/L$ is ''not too large,'' when T_f/z competes with T_*/z as an appropriate scale; (ii) σ_T^2 scales on T_f^2 (rather than T_*^2) so long as $-z_i/L$ is ''not too small,'' when Q_0 is so small that buoyancy forces are insignificant and temperature is a passive scalar, at which point $T_* = Q_0/u_*$ becomes the relevant scale; (iii) thus for $-z_i/L$ in the range where both shear and buoyancy contribute to buoyancy structure, mean and fluctuating temperature scale on different temperature scales near the ground. KB97 point out that $T_*/T_f = (-z/L)^{1/3} \gg 1$ when $-z/L \ll 1$.

Acknowledgments. The measurements at Marsta were performed within the framework of the NOPEX project. The airborne measurements and the radiosoundings during the 1994 campaign were financed by the Swedish Natural Research Council (NFR Contracts G-AA/GU 2684-312, 314, and 320). The airborne measurements during 1995 were financed by the Nordic Council of Ministers. The 1994 radiosoundings were made by Ph.D. students of the Department of Meteorology, Uppsala University. The radiosoundings during 1995 were made by a research group from University of Tsukuba, Japan, under the leadership of Dr. M. Sugita and kindly supplied by him. The airborne measurements were conducted by Dr. Michael Tjernström and Dr. Patrick Samuelsson of the Department of Meteorology, Uppsala University, and they were also evaluated by them. The analysis of the data was done within the framework of the Swedish Regional Climate Modelling Programme project, SWECLIM, which also financially supported the first author during part of the time.

JGB was supported by U.S. Army Research Office Grants DAAL03-92-G-0117 and DAAG55-97-1-0296.

APPENDIX

Determination of Gradients

Mean wind speed and potential temperature were measured at the following six levels on the tower: 0.84, 1.95, 4.78, 10.1, 17.2 and 29.0 m. This spacing is approximately logarithmic, the ratio of two consecutive heights being in the range 2.4–1.7. This choice was made because it is known that in neutral conditions profiles of any normalized mean quantity Q are expected to vary logarithmically with height z; that is, they will be represented by straight lines in a (Q, ln$z$) representation. For finite L values the profiles are expected to become slightly curved in this representation. Figure A1a shows a typical example of a wind profile and Fig. A1b the corresponding profile of potential temperature in this representation. The curves drawn in each graph are the respective best-fit second-order polynomials [Eq. (7a)] obtained by regression. It is seen that these curves are very good fits to the data. For this example the standard deviation between measured wind speed and the corresponding wind speed calculated from the regression expression is only 0.02 m s^{-1}. The corresponding mean standard deviation for all 156 half-hourly wind profiles against their respective regression equations is only 0.04 m s^{-1}. This figure compares well with the corresponding calibration uncertainty, which is estimated to about 0.05 m s^{-1}.

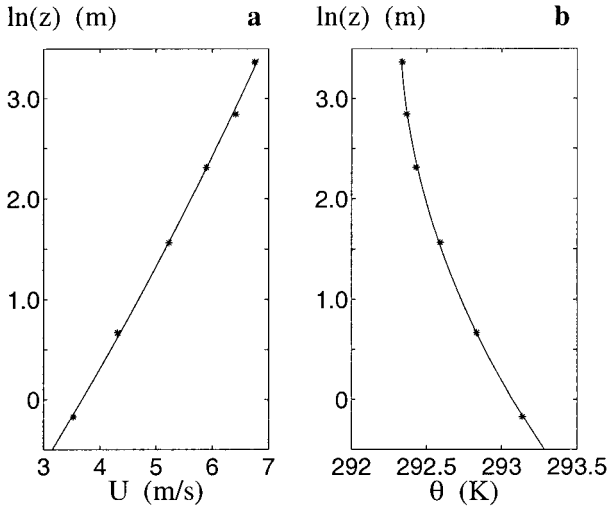

FIG. A1. Examples of 30-min mean profiles of (a) wind and (b) potential temperature against ln z from 1200 LST 21 Jun 1994. The measurements are indicated by stars and the curves are best-fit second-order polynomials in ln z [cf. Eq. (7a)]. The corresponding wind and potential temperature gradients are obtained from the differentiated form of the regression equations, Eq. (A1) for the turbulence measuring height, 10 m, corresponding to the level of the third star from the top of each profile.

The wind gradient has been obtained by differentiation of Eq. (7a) to give Eq. (7b), that is:

$$\frac{\partial U}{\partial z} = \frac{A}{z} + 2B\,\frac{\ln z}{z},$$

where z is set to 10 m, the height of the turbulence measurements. The accuracy of the wind gradient is thus dependent on the accuracy in the regression parameters A and B. But for the wind profile the second term is

typically an order of magnitude less than the first term, so we simplify the error analysis by looking only at the effect of the uncertainty in A. It can be shown that the error in A, ΔA is obtained by the following expression:

$$(\Delta A)^2 = \frac{s_q^2}{\sum x_i^2 - \left(\sum x_i\right)^2 \Big/ n},$$

where s_q^2 is the residual variance,

$$s_q^2 = \frac{1}{n-2} \sum_{i=1}^{n} (y_i - Ax_i - C)^2,$$

where $y_i = U_i$ and $x_i = \ln z_i$ with z_i indicating the measuring levels, so that $n = 6$.

The relative error in $\partial U/\partial z$ is then

$$|\Delta(\partial U/\partial z)|/(\partial U/\partial z) \approx |\Delta A|/(Az).$$

As a mean for all 137 half-hourly runs for which the second term of the regression equation (7) is less than 10% of the first term, this relative error in the wind gradient is 7.5%. For 19 of the profiles the second-order term is larger than 10%, so that the above simplified error estimation cannot be used. But the scatter of the data points around the best-fit curve for each of the profiles is not larger than for the more ''linear'' profiles. We therefore conclude that the estimate of the wind gradient in these cases is no worse than for the majority of the profiles.

The profiles of potential temperature are equally well defined as the wind profiles, mean standard deviation for all 156 half-hourly temperature profiles against their respective regression equations being only 0.007 K, which compares favorably with our calibration uncertainty for temperature differences, which is about $\pm$ 0.03 K. The potential temperature profiles are much more curved than the wind profiles, the second-order term of Eq. (7) being in the mean about 50% of the linear term. This makes a formal error analysis like the one performed above for the approximately linear (in the log representation) wind profiles much more complicated. It is, however, clear from the very good fit of the measured temperatures to the second-order polynomials in every individual case that the accuracy of the determination of the potential temperature gradient is equally good as that for the wind gradient, that is, the uncertainty is less than 10%.

REFERENCES

Banta, R. M., 1985: Late-morning jump in TKE in the mixed layer over a mountain basin. *J. Atmos. Sci.,* **42,** 407–411.

Bergström, H., and K. Lundin, 1993: Climatological mean wind and turbulence using a high quality cup anemometer system. *Proc. ECWEC '93,* Lübeck-Travemünde, Germany, Commission of the European Communities, 697–700.

Bradshaw, P., 1967: ''Inactive'' motion and pressure fluctuations in turbulent boundary layers. *J. Fluid Mech.,* **30,** 241–258.

Brown, E. N. C., C. H. Friehe, and D. H. Lenschow, 1983: The use of pressure fluctuations on the nose of an aircraft for measuring air motion. *J. Climate Appl. Meteor.,* **22,** 171–180.

Businger, J. A., J. C. Wyngaard, Y. Izumi, and E. F. Bradley, 1971: Flux–profile relationships in the atmospheric surface layer. *J. Atmos. Sci.,* **28,** 181–189.

Carl, D. M., T. C. Tarbell, and H. A. Panofsky, 1973: Profiles of wind and temperature from towers over homogeneous terrain. *J. Atmos. Sci.,* **30,** 788–794.

Deardorff, J. W., 1970: Convective velocity and temperature scales for the unstable planetary boundary layer and Raleigh convection. *J. Atmos. Sci.,* **27,** 1211–1213.

——, 1972: Numerical investigation of neutral and unstable planetary boundary layers. *J. Atmos. Sci.,* **29,** 91–115.

Dyer, A. J., 1974: A review of flux–profile relationships, *Bound.-Layer Meteor.,* **7,** 363–372.

——, and E. F. Bradley, 1982: An alternative analysis of flux–gradient relationships at the 1976 ITCE. *Bound.-Layer Meteor.,* **22,** 3–19.

——, and Coauthors, 1982: An international turbulence intercomparison experiment (ITCE 1976). *Bound.-Layer Meteor.,* **24,** 181–209.

Foken, T., and G. Skeib, 1983: Profile measurements in the atmospheric near-surface layer and the use of suitable universal functions for the determination of the turbulent energy exchange. *Bound.-Layer Meteor.,* **25,** 55–62.

Frenzen, P., and C. A. Vogel, 1992: The turbulent kinetic energy budget in the atmospheric surface layer: A review and an experimental reexamination in the field. *Bound.-Layer Meteor.,* **60,** 49–76.

Grelle, A., and A. Lindroth, 1994: Flow distortion by a Solent Sonic Anemometer: Wind tunnel calibration and its assessment for flux measurements over forest and field. *J. Atmos. Oceanic Technol.,* **11,** 1529–1542.

Halldin, S., L. Gottschalk, A. A. van de Griend, S.-E. Gryning, M. Heikenheimo, U. Högström, A. Jochum, and L-C. Lundin, 1998: NOPEX—A Northern Hemisphere climate processes land surface experiment. *J. Hydrol.,* **212–213,** 172–187.

Högström, U., 1988: Non-dimensional wind and temperature profiles in the atmospheric surface layer: A re-evaluation. *Bound.-Layer Meteor.,* **42,** 55–78.

——, 1990: Analysis of turbulence structure in the surface layer with a modified similarity formulation for near neutral conditions. *J. Atmos. Sci.,* **47,** 1949–1972.

——, 1996: Review of some basic characteristics of the atmospheric surface layer. *Bound.-Layer Meteor.,* **78,** 215–246.

——, A. Smedman, and H. Bergström, 1999: A case study of two-dimensional stratified turbulence. *J. Atmos. Sci.,* **56,** 959–976.

Hunt, J. C. R., 1984: Turbulence structure in thermal convection and shear-free boundary layers. *J. Fluid Mech.,* **138,** 161–184.

——, J. Kaimal, and J. E. Gaynor, 1988: Eddy structure in the convective boundary layer—New measurements and new concepts. *Quart. J. Roy. Meteor. Soc.,* **114,** 827–858.

Juneja, A., and J. G. Brasseur, 1999: Characteristics of subgrid–resolved-scale dynamics in anisotropic turbulence with application to rough-wall boundary layers. *Phys. Fluids.,* **11,** 3054–3068.

Kader, B. A., and A. M. Yaglom, 1990: Mean fields and fluctuations in unstably stratified turbulent boundary layers. *J. Fluid Mech.,* **212,** 637–661.

Kaimal, J. C., 1978: Horizontal velocity spectra in an unstable surface layer. *J. Atmos. Sci.,* **35,** 18–24.

——, J. C. Wyngaard, Y. Izumi, and O. R. Coté, 1972: Spectral characteristics of surface-layer turbulence. *Quart. J. Roy. Meteor. Soc.,* **98,** 563–589.

Khanna, S., and J. G. Brasseur, 1997: Analysis of Monin-Obukhov similarity from large-eddy simulation. *J. Fluid Mech.,* **345,** 251–286.

——, and ——, 1998: Three-dimensional buoyancy and shear-induced local structure of the atmospheric boundary layer. *J. Atmos. Sci.,* **55,** 710–743.

Lumley, J. L., and H. A. Panofsky, 1964: *The Structure of Atmospheric Turbulence.* Interscience Publishers, 239 pp.

Lundin, K., A. Smedman, and U. Högström, 1990: A system for wind and turbulence measurements in a wind farm. *Proc. ECWEC '90,* Madrid, Spain, Commission of the European Communities, 110–113.

Moeng, C.-H., 1984: A large-eddy-simulation model for the study of planetary boundary-layer turbulence. *J. Atmos. Sci.,* **41,** 2052–2062.

Monin, A. S., 1950: Turbulence in the atmospheric surface layer. *Coll. Sci. Inf. Hydrometeor. Ser. USSR,* **1,** 13–27.

——, and A. M. Obukhov, 1953: Dimensionless characteristics of turbulence in the atmospheric surface layer. *Dok. AN SSSR,* **93,** 223–226.

——, and ——, 1954: Basic laws of turbulent mixing in the ground layer of the atmosphere. *Tr. Geofiz. Inst., Akad. Nauk SSSR,* **151,** 163–187.

Obukhov, A. M., 1946: Turbulence in a thermally inhomogeneous atmosphere. *Bound.-Layer Meteor.,* **2,** 7–29.

Panofsky, H. A., H. Tennekes, D. H. Lenschow, and J. C. Wyngaard, 1977: The characteristics of turbulent velocity components in the surface layer under convective conditions. *Bound.-Layer Meteor.,* **11,** 355–361.

Paulson, C. A., 1970: The mathematical representation of wind speed and temperature profiles in the unstable atmospheric surface layer. *J. Appl. Meteor.,* **9,** 857–861.

Peltier, L. J., J. C. Wyngaard, S. Khanna, and J. G. Brasseur, 1996: Spectra in the unstable surface layer. *J. Atmos. Sci.,* **53,** 49–61.

Smedman, A., 1991: Some turbulence characteristics in stable atmospheric boundary layer flow. *J. Atmos. Sci.,* **48,** 856–868.

Stull, R., 1988: *An Introduction to Boundary Layer Meteorology.* Kluwer Academic Publishers, 666 pp.

Sullivan, P. P., J. C. McWilliams, and C.-H. Moeng, 1994: A subgrid scale model for large-eddy-simulation of planetary boundary-layer flows. *Bound.-Layer Meteor.,* **71,** 246–276.

Tennekes, H., 1982: Similarity relations, scaling laws and spectral dynamics. *Atmospheric Turbulence and Air Pollution Modelling,* F.T.M. Nieuwstadt and H. van Dop, Eds., D. Riedel Publishing Company, 37–68.

Tjernström, M., and C. A. Friehe, 1991: Analysis of radome air-motion system on a twin-jet aircraft for boundary-layer research. *J. Atmos. Oceanic Technol.,* **8,** 19–40.

Webb, E. K., 1982: Profile relationship in the superadiabatic surface layer. *Quart. J. Roy. Meteor. Soc.,* **108,** 661–688.

Willis, G. E., and J. W. Deardorff, 1974: A laboratory model of the unstable planetary boundary layer. *J. Atmos. Sci.,* **31,** 1297–1307.

Wyngaard, J. C., O. R. Coté, and Y. Izumi, 1971: Local free convection, similarity, and the budgets of shear stress and heat flux. *J. Atmos. Sci.,* **28,** 1171–1182.

——, L. J. Peltier, and S. Khanna, 1998: LES in the surface layer: Surface fluxes, scaling and SGS modeling. *J. Atmos. Sci.,* **55,** 1733–1754.

Yaglom, A. M., 1979: Similarity laws for constant-pressure and pressure-gradient turbulent wall flows. *Annu. Rev. Fluid Mech.,* **11,** 505–540.

Zilitinkevich, S. S., and D. V. Chailikov, 1968: Determining the universal wind-velocity and temperature profiles in the atmospheric boundary layer. *Izv., Atmos. Oceanic Phys.,* **4,** 165–170.

——, A. A. Grachev, and J. C. R. Hunt, 1998: Surface frictional processes and non-local heat/mass transfer in the shear-free convective boundary layer. *Buoyant Convection-in Geophysical Flows,* NATO ASI Series, E.J. Plate et al., Eds., Kluwer, 83–113.